Proceedings of Global Power and Propulsion Society
ISSN-Nr: 2504-4400
GPPS Hong Kong 2023
October 17-19, 2023
www.gpps.global

GPPS-TC-2023-0153

Study of a High-Pressure Ratio Centrifugal Compressor with a Wedge Diffuser and a Pipe Diffuser

Jun-nan Liu
School of Power and Energy, Northwestern Polytechnical University
dlljn@mail.nwpu.edu.cn
Xi'an, China

Xiuquan Huang
School of Power and Energy, Northwestern Polytechnical University
Xiuquan_huang@nwpu.edu.cn
Xi'an, China

ABSTRACT

A high-performance diffuser is crucial for a high-pressure ratio centrifugal compressor, as it dominates the flow downstream of the impeller. Pipe diffusers have been proved to be effective for high-pressure ratio centrifugal compressors. To understand the performance and flow mechanisms of pipe diffusers, an 8:1 pressure ratio centrifugal compressor is selected and a comparative study of compressor stages with a pipe diffuser and its original wedge diffuser was carried out using numerical simulations. At the design speed, the compressor with the pipe diffuser presents a better performance (lower total pressure loss, higher static pressure recovery and stable flow range) over the whole speedline than that with the wedge diffuser. The peak efficiency of the compressor with the pipe diffuser is 2.4 percentage points higher than that with the wedge diffuser. Compared with the wedge diffuser, the special scalloped leading edge of the pipe diffuser was found to reduce or even eliminate the flow distortion from upstream of the diffuser throat, which is beneficial to suppress the downstream flow separation.

Keywords: Pipe diffuser; Centrifugal compressor; Wedge diffuser; Numerical simulation; Leading edge

INTRODUCTION

Centrifugal compressors are widely employed in small aero-engines or gas turbines due to their capability of achieving higher single-stage total pressure ratio than axial compressors, allowing for more compact designs. However, centrifugal compressors often suffer from lower stage efficiency, which results from complicated secondary flow phenomena, particularly in the diffuser. This issue is particularly problematic in high-pressure ratio centrifugal compressors, where the diffuser inlet flow is often supersonic, resulting in significant shock loss and downstream flow deterioration. Therefore, it is crucial for researchers to understand the flow mechanisms of the diffusion system and design high-performance diffusers. The pipe diffuser, proposed by Vrana (1967) and Kenny (1969), has been verified to be a preferred choice for high-pressure ratio centrifugal compressors. It effectively mitigates the adverse effects of high inlet Mach numbers, handles highly distorted inlet flow, and offers cost-effective manufacturing. Both Pratt & Whitney (Bourgeois, 2009) and General Electric (Zachau, 2008) have adopted this diffuser type due to its high performance.

The pipe diffuser, as illustrated in Figure 1, similar to a traditional channel or a wedge diffuser, the pipe diffuser contains a vaneless space and a semi-vaneless space located ahead of the throat. Apart from these parts, the pipe diffuser features a unique region between the vaneless and semi-vaneless spaces, referred to as the pseudo-vaneless space. This region is formed by the interstation of two adjacent pipe passages and features a sharp leading edge known as the scalloped leading edge. Some investigations suggest that this specifically shaped leading edge has a remarkable function of adapting the high Mach number incoming flow, making it suitable for matching high-pressure ratio centrifugal impellers (Zachau, 2008; Kunte, 2013; Han, 2013). In this paper, we have gained a preliminary understanding of the scalloped leading edge by fluid field analyses.

Though previous research has provided valuable insights into flow characteristics (Daniel, 2013; Sugimoto, 2014; Han, 2023) and critical design parameters (Kenny, 1969; Reeves, 1977; Bennett, 1997; Han, 2014; Han, 2016; Yang, 2017), studies on the pipe diffuser for ultra-high pressure ratio centrifugal compressors are limited (Han, 2016; Han, 2023). Thus, conducting a further investigation is necessary. In this study, an 8:1 pressure ratio centrifugal compressor designed by NASA (Dolan, 1979) was selected as the research vehicle, numerical simulations of the centrifugal compressor with original wedge diffuser and pipe diffuser were carried out by the commercial code NUMECA FINE/OPEN. Detailed fluid

field analyses of the peak efficiency operating points for two diffusers were carried out to better understand the flow mechanisms.

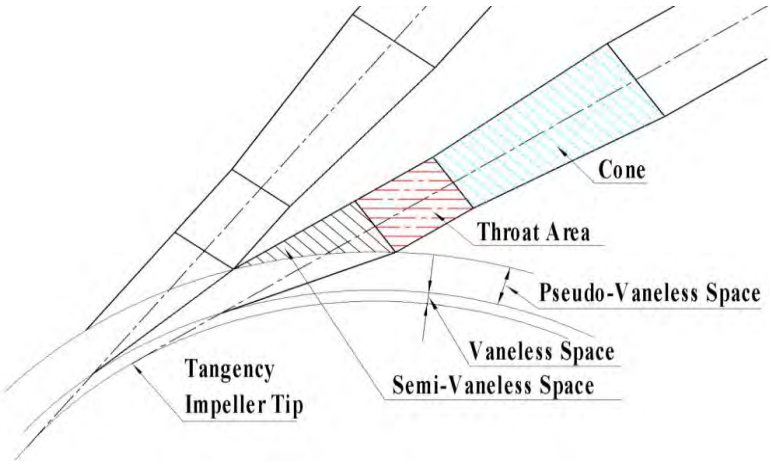

Figure 1 Schematic diagram of a pipe diffuser

CENTRIFUGAL COMPRESSOR STAGE AND THE PIPE DIFFUSER

Centrifugal compressor stage

The NASA high-pressure centrifugal compressor is comprised of two blade rows: an unshrouded backswept impeller and a wedge diffuser. The compressor geometry with its meridional cross section and essential design parameters are listed in Figure 2 and Table 1, respectively. In this paper, all analysis results and formula subscripts are based on the stations indicated in Figure 2 (b), encompassing the compressor with a pipe diffuser.

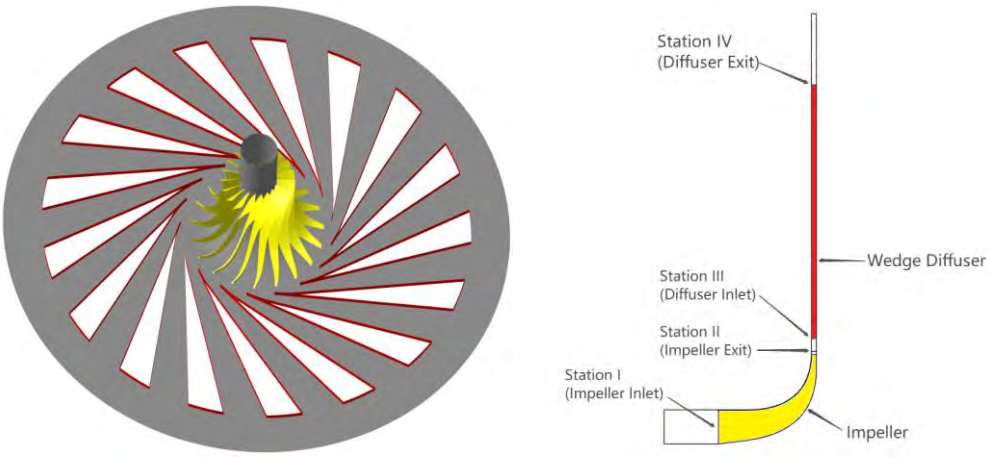

a) Three-dimensional geometry b) Meridional cross section

Figure 2 The NASA centrifugal compressor stage

Table 1 Design parameters of the NASA centrifugal compressor

Metrics	Value
Design speed (rpm)	75000
Impeller inner diameter (mm)	87.4
Impeller outer diameter (mm)	159.6
Impeller blade height at outlet (mm)	3.24
Tip speed (m/s)	626.7
Number of impeller blades	19
Blade back sweep angle (°)	30 (From radial)
Tip clearance (mm)	0.2
Wedge diffuser inner diameter (mm)	171.7
Wedge diffuser outer diameter (mm)	508
Wedge diffuser channel height (mm)	3.24

Number of wedge diffuser blades	17
Inlet metal angle (°)	72.26 (From radial)
Throat area (mm^2)	689.0
Divergence angle (°)	10
Area ratio (Outlet area/Throat area)	4.09

Pipe diffuser

The investigated pipe diffuser, designed based on the approach mentioned by Bennett (1997), is presented in Figure 3. Various parameters, such as the radius ratio of diffuser inlet to impeller exit (R_{III}/R_{II}), cross-sectional shape, number of diffuser passages (Np), diffuser throat area, diffuser throat length and divergence angle, can significantly affect the performance of the pipe diffuser. Thus, diffuser parameter recommendations provided by Kenny (1969), Bennett (1997) and Han (2014) were taken into account. It is important to note that R_{III}/R_{II} is kept the same as the wedge diffuser (1.076), which is slightly larger than the recommended value (1.04). Moreover, due to the small channel height (3.24mm) of the original wedge diffuser, the pipe diffuser with the same diameter requires approximately 85 diffuser passages to maintain a constant throat area. Therefore, the vaneless space had to be expanded to decrease Np. In the present work, the pipe diffuser throat diameter was designed as 5.7mm, ensuring Np falls within an appropriate range. The divergence angle in the vaneless space is approximately 60°, which will lead to inevitable flow separations. The detailed geometrical parameters are summarized in Table 2.

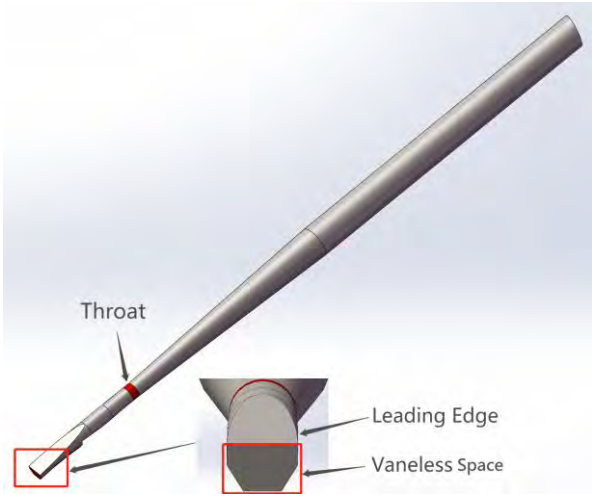

Figure 3 The pipe diffuser

Table 2 Design parameters of the pipe diffuser

Metrics	Value
Number of pipe diffusers	27
Pipe diffuser inner diameter (mm)	171.7
Pipe diffuser outer diameter (mm)	508
Throat length/Throat diameter	0.5
Divergence angle (°)	4
Diameter of the throat (mm)	5.7
Throat area (mm^2)	689.0
Inclination angle (°)	15.85
Area ratio (Outlet area/Throat area)	4.09
Cross-sectional shape	Circle

NUMERICAL DETAILS

Numerical method

Numerical simulations were carried out using the commercial computational fluid dynamics (CFD) software NUMECA FINE/OPEN, which is capable of solving both unstructured and structured multiblock grids. The explicit cell-centered finite volume scheme was used to solve the three-dimensional, compressible Reynolds-averaged Navier-Stokes Equations (RANS). Fourth order Runge-Kutta scheme was employed for temporal discretization, and one-equation Spalart-Allmaras (SA) (Spalart, 1992) turbulence model was chosen to enclose the governing equation. The multigrid procedure was employed to accelerate convergence.

Full-hexahedral structured meshes were generated for the original compressor using the commercial software NUMECA 13.2, AutoGrid5^{TM}. For the pipe diffuser, a hexahedral-dominated unstructured mesh was created using the commercial software NUMECA HexpressView. To satisfy the requirement of the SA turbulence model, the y^+ values on both the blade surfaces and end walls were maintained below 3.0. A grid independence study was conducted, encompassing both the impeller with a wedge diffuser and a pipe diffuser. The investigation comprised six grids, consisting of three grids with the impeller and a wedge diffuser, and three grids with the impeller and a pipe diffuser. The first cell width on solid walls remained constant for all grids to maintain the y^+ value. As illustrated in Figure 4, the total to static (T-S) isentropic efficiency (from station I to IV) and T-S pressure ratio are plotted versus the mass flow normalized by the measured choked flow, respectively. The converged maximum total pressure ratio point was treated as the near-stall point. It can be seen that the performance of both the finest and medium grids of two cases show nearly the identical results, with a difference in efficiency below 0.2% and closely matched pressure ratios. Hence, utilizing 3.2 million grid nodes for the original compressor and 3.86 million grid nodes for the pipe diffuser case strikes a well-balanced compromise between accuracy and computational cost. Single passage meshes of the original compressor and pipe diffuser chosen for investigation are depicted in Figure 5.

The determination of the heat capacity ratio for calculating isentropic efficiency is intricately linked to the total temperature. However, the ideal gas model assumes a constant heat capacity ratio. In light of this, when simulating high-pressure ratio compressors, the use of real gas becomes more appropriate than ideal gas, mainly due to the substantial temperature rise involved. Consequently, real air was chosen as the fluid material for both the compressor with a wedge diffuser and a pipe diffuser. The inlet boundary conditions were specified as a uniform total pressure of 101400Pa and a total temperature of 288.15K, while the inlet flow angle was set to zero in both the radial and circumferential directions. Static pressure was imposed at the diffuser exit, the compressor performance curves from choke point to near-stall point were simulated by varying the static pressure value. The non-slip and adiabatic wall conditions were applied to both blade surfaces and end walls, and the mixing plane was chosen to connect the impeller and diffuser.

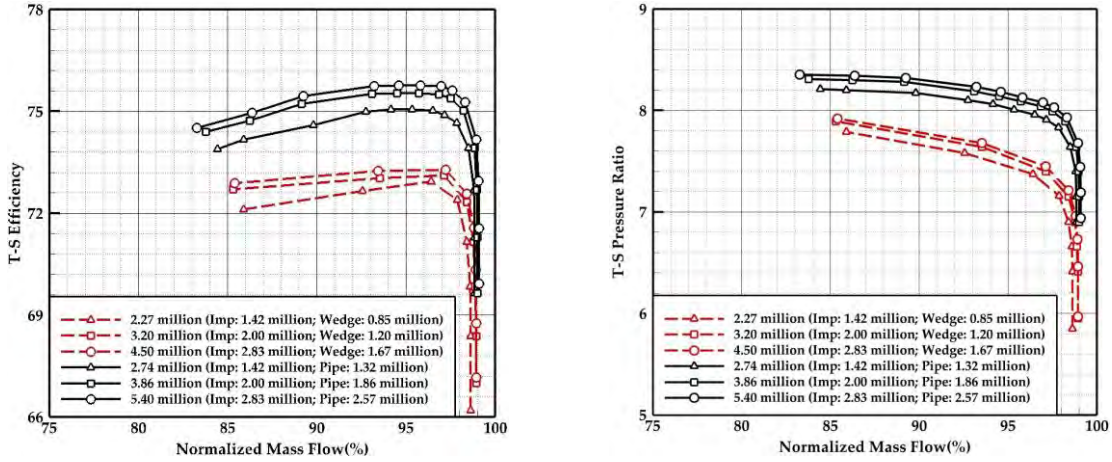

a) T-S isentropic efficiency b) T-S pressure ratio

Figure 4 Compressor performance characteristics with different grid configurations

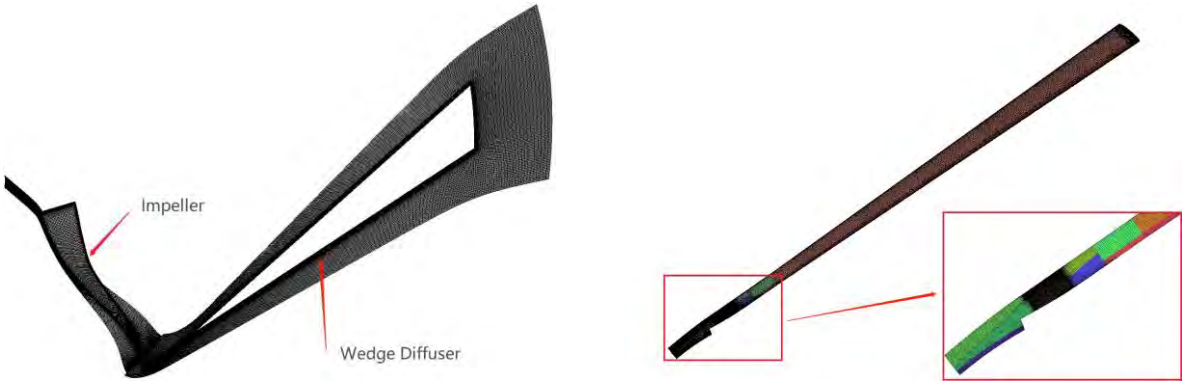

a) Original compressor grid b) Pipe diffuser grid

Figure 5 Computational grids of the NASA compressor with different diffuser configurations

Numerical validation

To validate the accuracy of the numerical simulations, a comparison between the original compressor numerical results and the corresponding measurement data was carried out. The compressor stage characteristics, including the T-S isentropic efficiency and T-S pressure ratio, were plotted against normalized mass flow at design and off-design speeds, as illustrated in Figure 6. It is evident that the performance curves closely match the measurement data at the design speed. As rotating speed decreases, both the mass flow range and pressure ratio exhibit good agreement with the measurement data, while the efficiency is somewhat underpredicted. Nevertheless, it is noteworthy that the efficiency curve obtained through numerical analysis follows the same trend as the measurement data. Consequently, the numerical method is deemed reasonable and reliable for predicting the flow phenomena within the NASA centrifugal compressor.

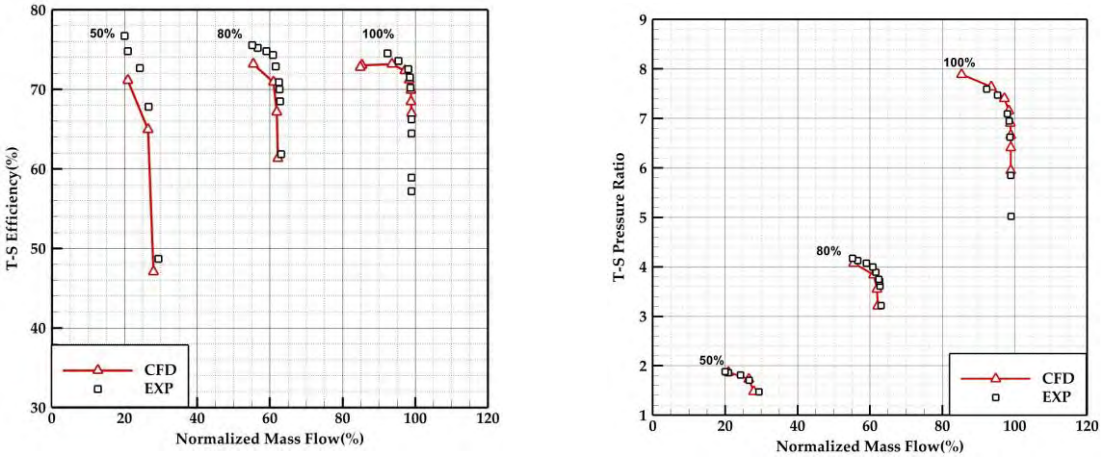

a) T-S isentropic efficiency b) T-S pressure ratio

Figure 6 Performance comparison between numerical simulation and measurement data

RESULTS AND DISCUSSION

Overall performance

Figure 7 illustrates the performance characteristics of the NASA centrifugal compressor with a wedge diffuser and a pipe diffuser at the design operating speed. The results demonstrate the superior performance of the compressor with a pipe diffuser in terms of T-S isentropic efficiency, T-S pressure ratio, and diffuser static pressure recovery coefficient (Cp) over the whole speed line. It should be noted that the circumferentially area-averaged static pressure and total pressure on Station II are used as a reference to calculate Cp and total pressure loss coefficient (TPL). Specifically, the peak efficiency of pipe diffuser is 2.4 percentage points higher than that of the wedge diffuser, and the pipe diffuser case has a wider stable flow range with a lower surge mass flow. However, it is important to acknowledge that the exaggerated expansion occurring in the pipe diffuser vaneless space leads to inevitable flow separation and subsequently results in higher TPL, as illustrated in Figure 7(d) II-III. Nonetheless, the pipe diffuser compensates for this limitation, as evidenced by the smaller TPL in Figure 7(d) II-IV when compared to the original compressor.

Hence, based on the results obtained at the design speed, the centrifugal compressor with a pipe diffuser appears to be more suitable than the one with a wedge diffuser, delivering better efficiency and a wider stable flow range. However, it is worth noting that the advantages of the pipe diffuser may diminish and even become inferior to the wedge diffuser as rotating speed decreases (Han, 2015). It is crucial to acknowledge that the present study only focuses on the design speed, and a thorough comparison of the off-design speed will be conducted in future research.

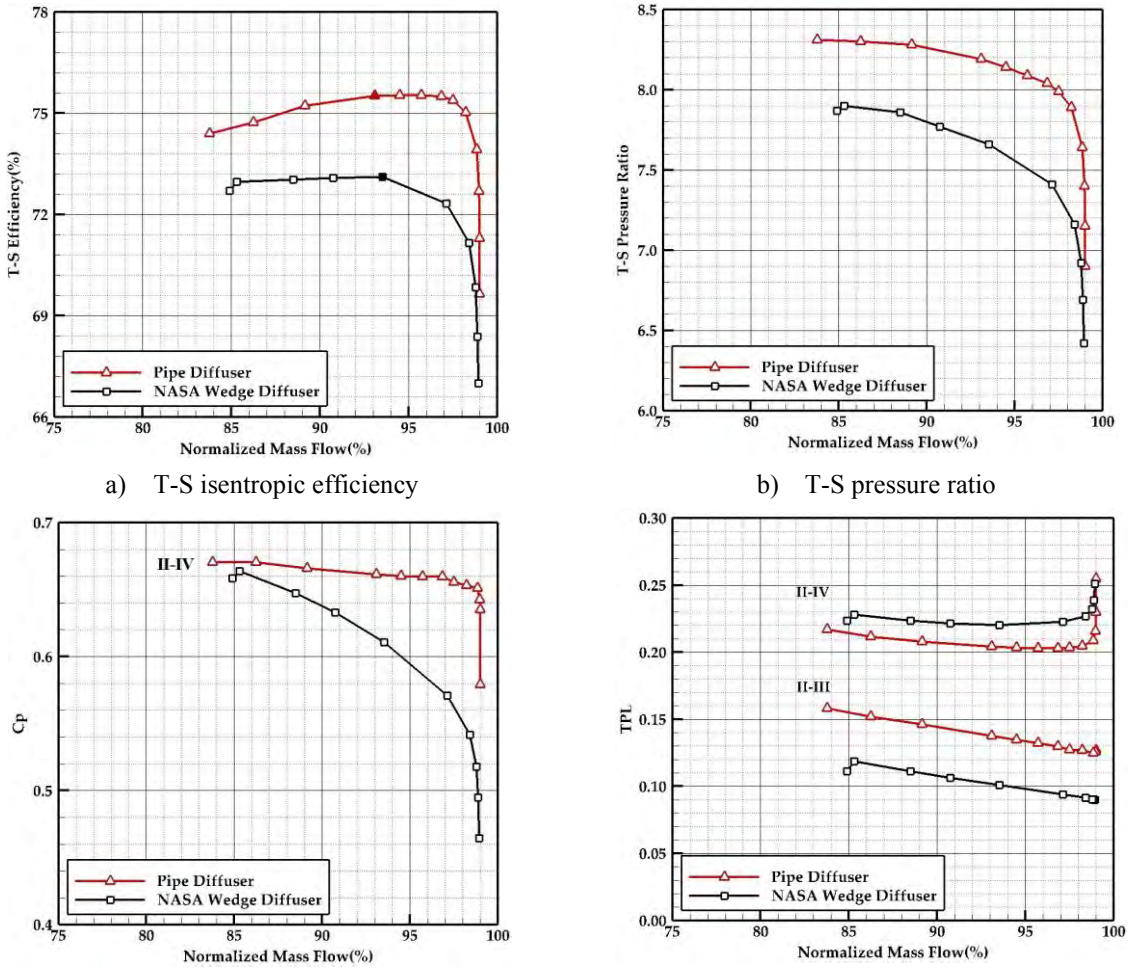

a) T-S isentropic efficiency

b) T-S pressure ratio

c) Static pressure recovery coefficient

d) Total pressure loss coefficient

Figure 7 Performance comparison between wedge diffuser case and pipe diffuser case

Analysis of the flow field at the peak efficiency operating points

In this section, a detailed flow field analysis was performed at the peak efficiency operating points for each diffuser, which are marked by solid dots in Figure 7(a).

To investigate the impact of the diffuser on the upstream flow, the relative Mach number distributions along the S3 surfaces (sections which are quasi-orthogonal to the channel centreline) of two impellers (one with a wedge diffuser and the other with a pipe diffuser) were examined and depicted in Figure 8. Remarkably, the Mach number distributions of the two impellers exhibit striking similarity, with both the shock wave and flow separations predicted at the same position. Furthermore, as depicted in Figure 9, it can be observed that both the original case and the pipe diffuser case exhibit nearly the same impeller pressure ratio curves. Therefore, it can be inferred that the type of diffuser has minimal effect on the flow field of the impeller, which is consistent with the report mentioned by Mohler (2005).

The vaneless space of the pipe diffuser attracts attention due to its larger TPL compared to the original compressor, as shown in Figure 7(d) II-III. Figure 10 presents the meridional streamlines, the TPL distribution against the normalized spanwise at station III and, the normalized radial velocity (normalized by the tip speed of the impeller) profiles against the normalized spanwise at station III for the two vaneless spaces, respectively. The excessive divergence angle in the pipe diffuser case leads to the formation of a large vortex near the shroud wall and a smaller vortex near the hub wall, as clearly observed in the meridional streamlines in Figure 10(a). The impact of this flow pattern is visually depicted in Figure 10(b), which exhibits a higher TPL over the whole spanwise for the pipe diffuser case compared to the original compressor, especially near the shroud. This figure directly illustrates the rationale behind the larger TPL observed in the pipe diffuser case as mentioned in Figure 7(d). In addition, as illustrated in Figure 10(c), it is evident that in the case of the pipe diffuser, there is a noticeable negative radial velocity in the vicinity of the shroud and hub regions. This corresponds to the flow separation bubbles shown in Figure 10(a). These huge bubbles play a significant role in the central flow region, leading to a more non-uniform velocity distribution when compared to the original case. Additionally, owing to the big expansion, the pipe diffuser case demonstrates a smaller radial velocity over the whole spanwise than the original case.

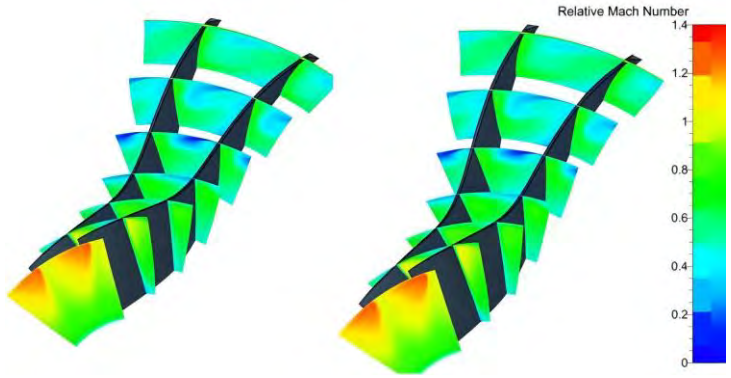

Figure 8 Relative Mach number distributions of impellers (Left: wedge diffuser; right: pipe diffuser)

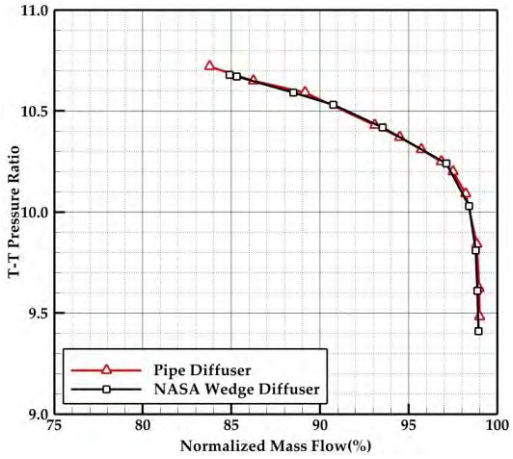

Figure 9 Pressure ratios of two impellers

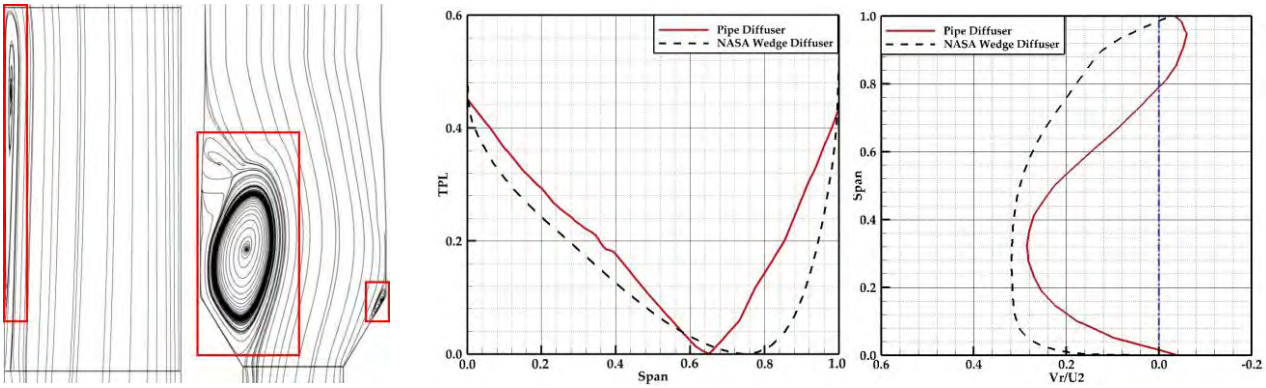

a) Meridional streamlines of vaneless spaces

b) TPL distribution profile at station III

c) Radial velocity profiles at station III

Figure 10 Comparison of vaneless spaces between the wedge diffuser and pipe diffuser cases

To conduct a comprehensive analysis, eleven cross-sections were selected along the passage of the pipe diffuser, as illustrated in Figure 11. These cross-sections, labelled as station 01 to station 11, cover various regions of the pipe diffuser. Station 01 represents the plane near the diffuser inlet. Station 01 to 04 denotes the pseudo-vaneless space, while station 04 is located on the scalloped leading edge of the elliptical ridges. Station 04 to 05 correspond to the semi-vaneless space. Station 05 and station 06 are positioned at the throat inlet and outlet, respectively. Station 11 is located near the exit of the pipe diffuser passage. Furthermore, these eleven stations are also utilized for the wedge diffuser. However, since the pipe diffuser has a unique structure, some stations such as the throat outlet (station 06) only exist in the pipe diffuser, whereas for the wedge diffuser, these stations are included solely for comparison purposes.

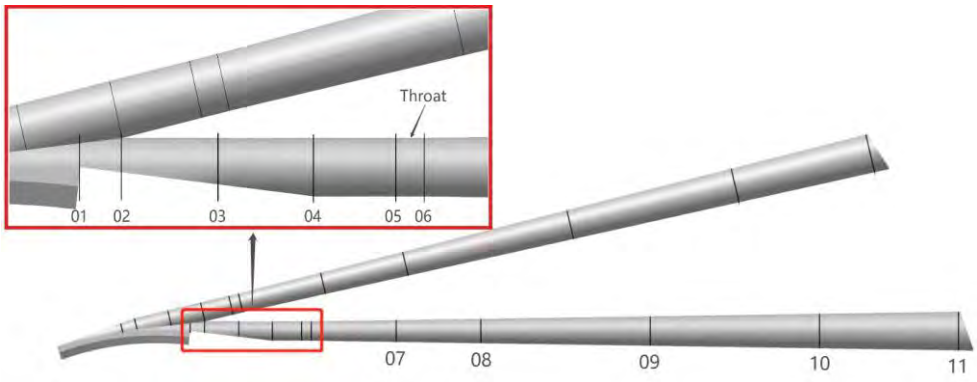

Figure 11 Selected cross-sections of the pipe diffuser

Figure 11 presents the Cp, TPL, and absolute Mach number (AbsMa) profiles at eleven stations along the passage of the original compressor and pipe diffuser case, including the impeller exit (Station II). The Cp and TPL values are

calculated with reference to the circumferentially area-averaged static pressure and total pressure at Station II, allowing for a comprehensive comparison of the flow characteristics and performance between the two configurations.

Compared with the original compressor, it is noteworthy that the pipe diffuser case exhibits a significant increase in both Cp and TPL from station II to station 01. This is attributed to the sudden expansion in the vaneless space, causing a rapid flow deceleration and subsequent static pressure rise. However, as previously mentioned, this region is characterized by the presence of a large vortex near the shroud wall, leading to a substantial total pressure loss.

Between station 01 to 03, flow acceleration and a reduction of TPL can be observed. As the flow develops, the adverse effects of the vaneless space gradually diminish, and the high-energy flow dominates the main flow, leading to an increase in total pressure and flow acceleration. From section 03 to 05, the adverse effects of vaneless separation become almost negligible, and the pipe diffuser begin to diffuse. However, the advantages of pipe diffuser are not yet evident in this region, as the rate of Cp increase is nearly the same as that of the wedge diffuser.

For the pipe diffuser, the static pressure recovery remains almost constant at the throat region, with a slight total pressure loss. Due to the constant throat area from station 05 to station 06 and the fully developed boundary layer, so there is a slight decrease in flow velocity (shown in Figure 12(b)) caused mainly by friction losses. After throat (station 06), the pipe diffuser continues to diffuse, and the advantage of the pipe diffuser over the wedge diffuser becomes increasingly apparent.

From station 07 to 11, the pipe diffuser shows higher static pressure recovery and lower total pressure loss than the wedge diffuser. The rate of Cp rise for the wedge diffuser tends to stabilize, while for pipe diffuser, it continues to rise slowly. Furthermore, as illustrated in Figure 12(b), the pipe diffuser experiences a rapid deceleration after the throat, resulting in a lower exit velocity compared to the wedge diffuser. Despite suffering from huge vortices in the vaneless space, the pipe diffuser is expected to outperform than the wedge diffuser in terms of flow deceleration and pressure rise.

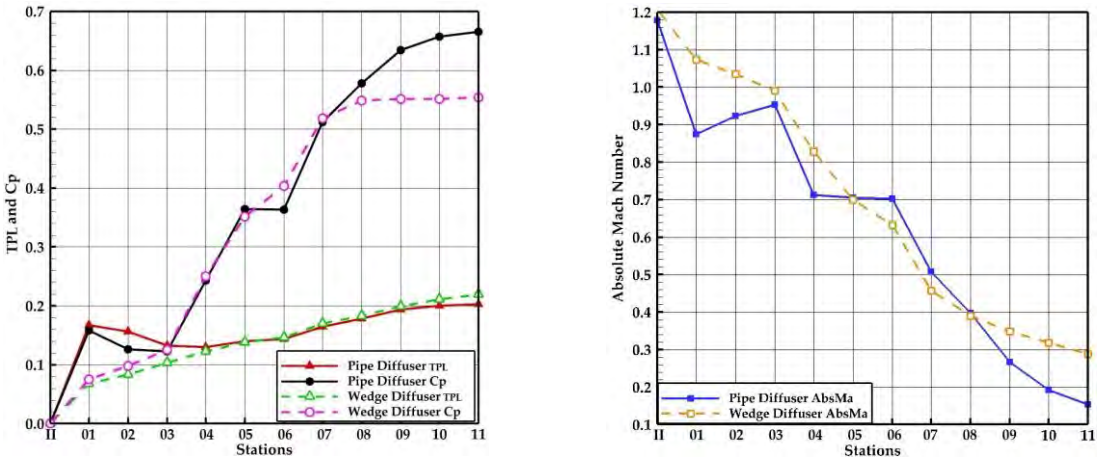

a) Cp and TPL b) Absolute Mach number

Figure 12 Profiles of various parameters at peak efficiency points along selected stations

Figure 13 depicts the distribution of absolute Mach number and surface streamlines at the midspan. For the wedge diffuser, a strong shock wave is observed near the leading edge, the low-momentum flow starts to congregate at the diffuser throat and cannot be effectively suppressed. Consequently, as the diffuser channel expands, the flow downstream deteriorates gradually, with low-momentum flow gathering on the pressure side and flow separation is triggered in the diffuser channel. However, the Mach number in the pipe diffuser is lower than that in the wedge diffuser from inlet to the leading edge, and almost no flow separation could be found in the diffuser passage due to its special leading edge.

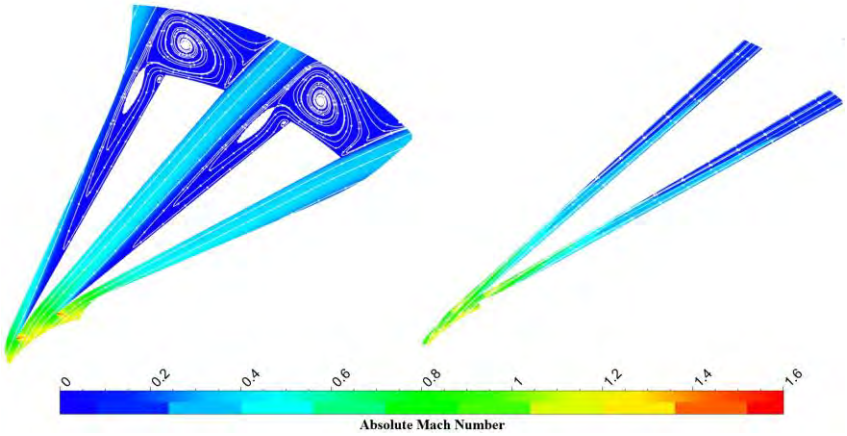

Figure 13 Absolute Mach number contours and streamlines at 50% span

(Left: wedge diffuser; right: pipe diffuser)

To track the evolution of vortices within the pipe diffuser and gain a deeper understanding of the scalloped leading edge, the distribution of entropy along with the surface streamlines at eleven stations (shown in Figure 11) are investigated, as exhibited in Figure 14. In this paper, following the derivation of Denton (1993), the entropy is non-dimensionalized by the compressor work input, the formula is shown as follows:

$$S_{Dimensionless} = \frac{T_{tI} S}{C_p (T_{tI} - T_{tI})}. \qquad (1)$$

Where Cp is the heat capacity, S the entropy. At station 01, due to the influence of vortices in the vaneless space close to the shroud wall, the low-momentum flow is mainly concentrated in the region from midspan to the shroud. Although the low-momentum fluid near the shroud wall deviates towards the suction side (SS), it tends to move from SS to the pressure side (PS) due to flow deflection caused by incidence, then redirected again and moves along the shroud wall from SS to PS. Hence, we can find a clockwise vortex at the shroud corner close to the SS. As the flow progresses, the impact of the vaneless space gradually diminishes, and the high-energy fluid moves from hub to the near shroud wall, reclaiming a dominant position in the passage. Consequently, the corner vortex is suppressed by the main flow, and almost disappear in station 03. The predominated high-energy fluid brings an increased total pressure and flow acceleration from station 01 to station 03, which has been exhibited in Figure 12.

At station 04, as the flow move across the elliptical ridge of the scalloped leading edge, two vortices with opposite moving trajectories are generated near the PS, the vortex near the shroud wall (VS) is larger than the one near the hub wall (VH). As observed at station 03, the predominant vortex demonstrates a counterclockwise movement from the hub to the shroud wall and, with the impact of the different incidence from the hub to shroud span. Consequently, despite it is divided into two parts, the vortex near the shroud wall maintains a predominant position. These two vortices, especially VS, effectively transport both the rich-energy and low-momentum flow near the PS (highlighted within the red rectangle) into the main flow, directing them along a counterclockwise path near the diffuser wall towards the PS. This process re-energizes the low-momentum flow, leading to a reduction in aerodynamic loading and contributing to the improved performance of the pipe diffuser compared to the wedge diffuser. Moving from station 04 to 06, the high-energy flow in VH gradually transitions to VS, resulting in a significant growth and intensifications of VS. As a result, the pair vortices mix into a single vortex which occupies nearly the entire section at station 07. It is hard to determine whether this single vortex retains the ability to transport low-momentum flow near the PS. However, it continues to transport the mixed flow from PS to PS until the flow reaches the exit of the pipe diffuser.

Finally, the mass-averaged dimensionless entropy along each section is plotted to illustrate the entropy change, as shown in Figure 15. It is seen that the trend of entropy distribution closely resembles the TPL profile presented in Figure 12. The significant entropy rises from station 0 to station 01 can be attributed to the huge separation in the vaneless space. In station 01 to station 04, the impact of the vaneless space gradually diminishes and, the energy is redistributed, leading to the entropy reduction. Within the throat area (station 05 to station 06), the entropy remains constant. At station 07, a rise in entropy is noticeable due to the mixing of two vortices and the friction losses. From station 08 to station 11, the entropy continues to rise, primarily driven by friction losses.

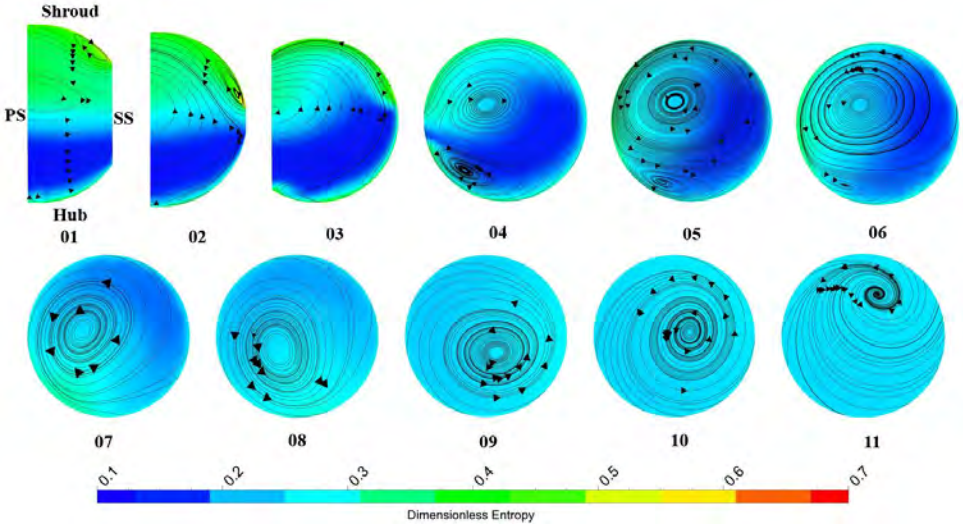

Figure 14 Entropy distribution and streamlines at various stations in the pipe diffuser

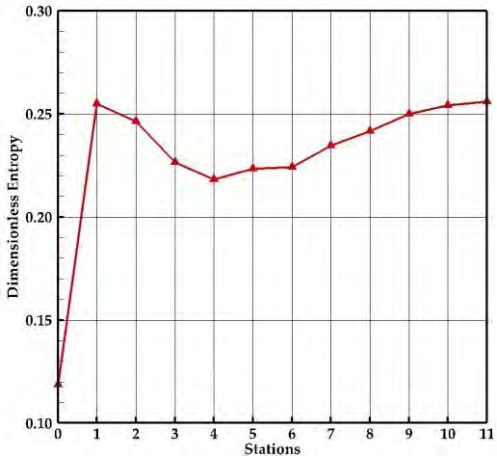

Figure 15 Profile of the pipe diffuser entropy distribution along selected stations

CONCLUSIONS

In order to comprehensively understanding the performance and flow mechanisms of pipe diffusers, a comparative study of an 8:1 pressure ratio centrifugal compressor with a pipe diffuser and its original wedge diffuser was conducted through numerical simulations. The compressor with the pipe diffuser exhibits better aerodynamic performance (lower total pressure loss, higher static pressure recovery and stable flow range) over the whole speedline compared to the original compressor. The peak efficiency operating points of two diffuser cases were selected for detailed analyses. The main conclusions of the present work can be drawn as follows:

1) The pipe diffuser is expected to perform better than the wedge diffuser in terms of flow deceleration and mitigating the adverse effects of the shock wave, which possesses a better capability of diffusion.
2) In the wedge diffuser, the combination of a strong shock wave and channel expansion resulted in continuous deterioration of flow separation, limiting its diffusion capabilities in the second half of the channel.
3) For the pipe diffuser, the counter-rotating pair vortices generated by the scalloped leading edge can transport and re-energize the low-momentum flow near the pressure side. This re-energized flow was then redirected back to the pressure side, effectively suppressing distortions from the upstream diffuser throat and facilitating further flow development.

Considering the two vortices depicted in Figure 14, the vortex near the hub wall (VH) contributes to transporting low-momentum flow into the main flow region and mixing it with the high-energy flow. However, due to the influence of incidence, this vortex is smaller compared to the other one (VS). Hence, the author proposes that some strategies, such as adjusting the blade metal angle, could be employed to enhance this vortex. This, in turn, could potentially prove beneficial in improving the performance of the pipe diffuser.

Further work should focus on conducting detailed flow analyses the near choke and stall points at the design speed. Additionally, investigating the impact of off-design speed on the performance of the pipe diffuser through numerical simulations would be beneficial.

NOMENCLATURE

CFD	Computational fluid dynamics
Cp	(1) Static pressure recovery coefficient, $Cp = (P_s\text{-}P_{s,\,ref})/ (P_t\text{-}P_{t,\,ref})$
	(2) Heat capacity
Np	Number of pipe diffuser passages
R	Radius
RANS	Reynolds-averaged Navier-Stokes equations
rpm	Revolutions per minute
S	Entropy
T_t	Total temperature
y^+	Dimensionless wall distance

Subscripts

I	Impeller inlet
II	Impeller exit
III	Diffuser inlet
IV	Diffuser exit

P	Pressure
ref	Reference
s	Static
t	Total

Abbreviation

AbsMa	Absolute Mach number
PS	Pressure side
SA	Spalart-Allmaras
SS	Suction side
TPL	Total pressure loss coefficient, TPL = 1 - P_t/ $P_{t, ref}$
T-S	Total to static
T-T	Total to total
VH	Vortex near the hub wall
VS	Vortex near the shroud wall

REFERENCES

Bennett, I. (1997). *Design and analysis of pipe diffuser for centrifugal compressor*. Ph.D. Cranfield University.

Bourgeois, J. A., Martinuzzi, R. J., Roberts, D., et al. (2009). Experimental and numerical investigation of an aero-engine centrifugal compressor. In: *ASME Turbo Expo 2009: Power for Land, Sea and Air*, Florida, USA.

Daniel, R. G., Peter, J., Reinhard, N. (2013). Numerical investigation of the unsteady flow inside a centrifugal compressor stage with pipe diffuser. In: *ASME Turbo Expo 2013: Turbine Technical Conference and Exposition*, Texas, USA.

Denton, J. D. (1993). The 1993 IGTI scholar lecture: Loss mechanisms in turbomachines. *Journal of Turbomachinery*, **115**(4), pp. 621-656.

Dolan, F. X., Runstadler, P. W. (1979). Design, development, and test of a laser velocimeter for a small 8:1 pressure ratio centrifugal compressor. NASA/CR-134781.

Han, G., Lu, X. G., Zhao, S. F., et al. (2014). Parametric studies of pipe diffuser on performance of a highly loaded centrifugal compressor. *Journal of Engineering of Gas Turbine and Power*, **136**(12), pp. 122604-1-9.

Han, G., Lu, X. G., Zhang, Y. F., et al. (2015). Study of a highly loaded centrifugal compressor with pipe diffuser at design and off-design operating conditions. In: *ASME Turbo Expo 2015: Turbine Technical Conference and Exposition*, Montreal, Canada.

Han, G., Lu, X. G., Zhang, Y. F. (2016). Study of geometric parameter influence on fishtail pipe diffuser performance. In: *ASME Turbo Expo 2016: Turbomachinery Technical Conference and Exposition*, Seoul, South Korea.

Han, G., Yang, C. W., Wu, S. X., et al. (2023). The investigation of mechanisms on pipe diffuser leading edge vortex generation and development in centrifugal compressor. *Applied Thermal Engineering*, **219**, 119606.

Kenny, D. P. (1969). A novel low-cost diffuser for high-performance centrifugal compressor. *Journal of Engineering of Gas Turbine and Power*, **91**(1), pp. 37-47.

Kunte, R., Schwarz, B., Wilkosz, B. (2013). Experimental and numerical investigation of tip clearance and bleed effects in a centrifugal compressor stage with pipe diffuser. *Journal of Turbomachinery*, **135**(1), 011005-1-011005-12.

Mohler, S. R. Jr. (2005). Wind-US unstructured flow solutions for a transonic diffuser. NASA/CR-213417.

Reeves, G. B. (1977). Design and performance of selected pipe-type diffusers. In: *Proceeding of Gas Turbine Conference and Products Show*, Philadelphia.

Spalart, P. R., Allmaras, S. R. (1992). A one-equation turbulence model for aerodynamic flow. AIAA Paper-92-0439.

Sugimoto, T., Kawanishi, T., Kumamaru, H., et al. (2014). Performance investigation into supersonic diffuser for a high pressure centrifugal compressor. In: *ASME Turbo Expo 2014: Turbine Technical Conference and Exposition*, Germany.

Vrana, J. C. (1967). *Diffuser for centrifugal compressor*. US3333762.

Yang, X., Jin, D. H., Gui, X. M. (2017). Aerodynamic design and optimization of pipe diffuser for a high-loading centrifugal compressor. In: *Fluid Engineering Division Summer Meeting*, Hawaii, USA.

Zachau, U., Buescher, C., Niehuis, R., et al. (2008). Experimental investigation of a centrifugal compressor stage with focus on the flow in the pipe diffuser supported by particle image velocimetry (PIV) measurements. In: *ASME Turbo Expo 2008: Power for Land, Sea and Air*, Berlin, Germany.